[1]T. Kalaichelvi
[1]S. Ravi
[2] Buddepu Santhosh Kumar
[3] Saranya A.

# Enhancing Landmine Detection Using Deep Learning: Leveraging AlexNet for Classification

Journal of Electrical Systems

**Abstract:** Landmine detection is the biggest challenge today, especially with the explosion of anti-tank and anti-personnel landmines, bombs, and unexploded ordnance. Many countries around the world are at risk from buried landmines. Various techniques automatically detect and recognize subsurface objects. However, they have limitations and must be more reliable when applied to all soils with different mediums to provide accurate results. Ground penetrating radar (GPR) uses electromagnetic signals to identify subsurface objects, and it detects landmines deeper with minimal metallic content than other sensors. Advances in deep learning techniques could revolutionize anti-personnel landmine detection and classification, demonstrating incredible results with high accuracy rates. The paper explores applying the deep learning approach (AlexNet) architecture using simulated GPR data to enhance the identification of landmines and similar underground objects. This study utilizes gprMax software to simulate the GPR data of buried objects. Subsequently, the data is implemented and analyzed within the MATLAB environment. Our findings demonstrate that AlexNet outperforms a standard convolutional neural network (CNN) model, achieving higher accuracy, precision, recall, and F1 scores in classifying metal pipes, metal tiffin boxes, and plastic tiffin boxes buried underground. It highlights the potential of deep learning for landmine detection using GPR data.

***Keywords:*** AlexNet, Convolutional Neural Network, Ground Penetrating Radar, Landmine Detection, Subsurface Objects

## I. INTRODUCTION

Landmines claim countless lives and livelihoods every year. They pose a serious threat to civilians, causing severe injuries and loss of life. There is a critical need to develop faster and more accurate landmine detection methods and technologies [1]. More than 60 countries and territories are still suffering from landmines, which continue to kill and injure civilians, destroy livelihoods, deny land use, and disrupt essential services [2]. Landmine Monitor 2022 reported that 117,350 anti-personnel landmines were cleared and destroyed worldwide in 2021. Around 5,544 casualties from landmines, explosive remnants of war (ERW), and improvised explosive devices (IEDs) were reported, including 2,182 deaths; half of those killed or maimed were children [3]. Metal detectors are a standard method that struggles to identify landmines with low metal content, and they are prone to generating false positives due to harmless metal objects in the soil [4]. Traditional landmine detection methods, such as metal detectors, can be unreliable depending on the soil composition and the type of landmine. Furthermore, soil conditions such as moisture levels, mineral content, and electrical conductivity can significantly hinder the effectiveness of metal detectors [2].

GPR emerges as a breakthrough technology in landmine detection. It offers a non-intrusive approach to identifying buried objects such as metals, concrete, pipes, landmines, cables, etc., [5], especially those with low metal content, by analyzing their unique electromagnetic (EM) signature. GPR emits EM waves into the subsurface and examines the reflected signals to identify anomalies caused by buried objects exhibiting different dielectric properties than the surrounding soil [6]. The technology holds promise for deeper detection of landmines, particularly those with minimal metallic content. The transmitter antenna starts with individual radar traces known as A-scans. The process continues with consecutive radar traces in a specific direction, termed B-scans,

[1,3] Department of Computer Science, School of Engineering and Technology, Pondicherry University, Puducherry, India
Email：assertivekalai@gmail.com , *sravicite@pondiuni.ac.in , sharansasi1896@gmail.com
[2] Department of Electronics and Communication, Amrita School of Engineering, Amrita Vishwa Vidyapeetham, Andhrapradesh,
Email：b_santhoshkumar@av.amrita.edu

culminating in generating a set of B-scan images [7]. GPR mainly identifies buried objects, detects subsurface structures using EM waves, and visualizes them as hyperbolic patterns [8]. It is also widely used in geology, archeology, civil, environmental, military, and mining applications. Figure 1 shows the components of the GPR process.

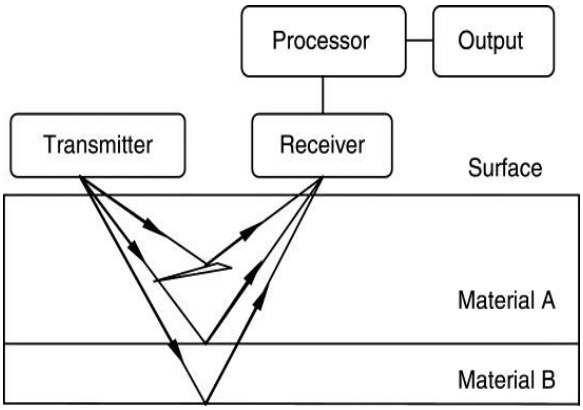


**Figure 1. Components of Ground Penetrating Radar [9]**

The paper explores applying deep learning techniques for landmine classification using GPR data, specifically a deep convolutional neural network (DCNN) architecture called AlexNet. Deep learning has demonstrated significant achievements in image recognition tasks, and this research investigates its potential to revolutionize landmine detection by enhancing the accuracy and effectiveness of GPR data analysis.

## II. DEEP LEARNING TECHNIQUES FOR LANDMINE DETECTION USING GPR IMAGES

Deep learning is vital in identifying and classifying landmines, especially when dealing with noisy and cluttered GPR data. Deep learning techniques help interpret data better, mainly when there's a lot of environmental and experimental noise. Researchers have increasingly explored CNN-based methods to recognize hyperbolas and classify buried objects in GPR data. These methods excel at finding detailed patterns and features in GPR images, which help detect and classify buried landmines more accurately. Table 1 presents landmine detection results using a CNN technique utilizing GPR B-Scan Images.

**Table 1**
**Landmine detection based on CNN technique using GPR B-Scan Images**

| Year | Author | Technique | Dataset | Metrics |
|---|---|---|---|---|
| 2015 | L.E. Besaw et al., [10] | SVM | AP, AT mines | Pd - 0.9 |
| 2017 | S.Lameri et al., [11] | Data-driven | Simulated | Acc - 95% |
| 2018 | M.T. Pham et al., [12] | RCNN, HOG, and Haar-like | Real, Simulated | CI - 0.7 |
| 2019 | N.Kim et al., [13] | DCNN | Real | Acc - 98% |
| 2019 | H. Harkat et al., [14] | MOGA, RBF | Real | Acc - 89% |
| 2020 | M. Elsaadouny et al., [15] | LeNet-5 | Fashion-MNIST | Acc - 95% |
| 2020 | U. Ozkaya et al., [16] | CSVM | Simulated | Acc - 95% |
| 2021 | F. Hou et al., [17] | Mask-CNN, DGIoU | Real | Acc - 58% |
| 2022 | P.Srimuk et al., [18] | MRCNN, SVM | Real | IoU - 91% |
| 2022 | H.Wang et al., [19] | DCNN, GAN | Simulated | EI - 93 % |
| 2022 | N. Barkataki et al., [20] | Scharr Operator | Simulated | VL - 9.87 |
| 2023 | M. Wang et al., [21] | SPDM, LARM | Real, Synthetic | P - 96.2% |
| 2023 | H. Liu et al., [22] | YOLOv3 | Real | P - 95.6% |
| 2023 | Z. Wang et al., [23] | RCNN | Synthetic, Sandbox | MSE - 3637.31 |
| 2024 | H. Fang et al., [24] | SimTrans-GPR | Annotated | Acc - 87.62% |

L. E. Besaw et al. [10] employed a support vector machine (SVM) to detect buried explosive hazards

(BEHs) and false alarm (FA) signatures in B-scan images of GPR. They achieved better detection with fewer false alarms but needed more precise visualization of subsurface objects. S. Lameri et al. [11] worked on small, highly accurate image patches but required different antenna polarizations. M.T. Pham et al. [12] adopted hyperbola reflections to detect buried objects using a region-based convolutional neural network (RCNN) with a high confidence index (CI). They used a histogram of oriented gradients (HOG) and Haar-like feature extraction compared to the cascade object detector (COD). N. Kim et al. [13] used C-scan GPR data to classify underground objects using DCNN. They reduced false positives, which is crucial for urban areas.

H. Harkat et al. [14] selected features using the radial basis function (RBF) using a multi-object genetic algorithm (MOGA) and classified them with and without target images. M.Elsaadouny et al. [15] implemented LeNet-5 CNN trained with a larger dataset of Fashion-MNIST, comparing results with transfer learning from the GPR dataset. Transfer learning appeared more effective but required further research. U. Ozkaya et al. [16] developed a convolutional support vector machine (CSVM) classification method to identify materials used for buried objects, reducing training time by incorporating more real-world GPR B-Scan images and multitask learning. F. Hou et al. [17] implemented a mask region-based CNN (MRCNN) with Distance-Guided Intersection over Union (DGIoU) for accurately detecting hyperbolic signatures of rebars in GPR images.

P. Srimuk et al. [18] implemented automatic detection of buried IEDs using an RCNN based on GPR B-Scan image hyperbolic patterns. It performed well but required preprocessing for GPR images. H. Wang et al. [19] used a DCNN as a multilayer feature fusion network to extract image feature maps. Generative adversarial networks (GAN) generated realistic GPR B-SCAN images for better GPR target detection. They calculated the evaluation index (EI) based on precision (P) and recall (R) to improve target detection accuracy. N. Kim et al. [25] involved 2D grid images with B and C-scan images to train DCNN for subsurface object classification, validated with field data from South Korea. N. Barkataki et al. [20] used a CNN model to estimate the size of subsurface objects. They processed simulated data with Sobel, Laplacian, Scharr, and Canny operators to detect top-level hyperbolic properties. The Scharr operator performed best with ten hidden layers.

M. Wang et al. [21] developed a deep learning network for precise pipeline size and location detection, incorporating simultaneous localization and mapping (SLAM) for GPR position estimation. Their approach, employing the subsurface pipeline detection module (SPDM) alongside the localization and aboveground reconstruction module (LARM) framework, yielded high precision. H. Liu et al. [22] utilized You Only Look Once version 3 (YOLOv3) to locate underground pipelines. They estimated a pipeline's buried position and depth by transforming hyperbolic responses into binary images. Z. Wang et al. [23] successfully reconstructed defect signals of rebars using unsupervised learning. They achieved low mean square error (MSE) with simulated data and moderate MSE with real-world noise. The CNN-based deep learning models presented here use different techniques, such as B and C-Scan images of landmines. H. Fang et al., [24] employed weak-shot learning for the classification of pipelines, and the model has reliable in cross-domain transfer learning.

The landmine detection techniques used actual data from minefields and landmine-free areas. In the study, the authors utilized synthetically generated data and data acquired from controlled sandbox experiments. Notably, researchers have increasingly employed artificially generated GPR data, created using simulation tools like GprMax, to classify underground objects [12], [17], [25], [21].

A LeNet architecture was proposed [11] and trained on real GPR data. The evaluation showed that a LeNet model using a patch size of 64 achieved 95% accuracy and 97% Area Under the Curve (AUC). [25] retrieved B and C-scan images from multichannel GPR to generate the 2D image grid for classification using deep neural network produced 98% accuracy. The CNN model [15] implemented LeNet-5 trained with fashion MNIST dataset and made with the highest precision and accuracy. YOLOv3 was adopted [22] to recognize the underground pipelines and attained less error. Studies have employed various CNN architectures and techniques, including RCNNs, LeNet, and SVM integration, achieving promising results. However, challenges remain, particularly the limited availability of real-world GPR data for training and validation.

## III. PROPOSED METHODOLOGY

### 3.1 Simulated GPR Data Acquisition

gprMax, an open-source GPR simulation software that utilizes GPU acceleration, was used to generate B-scan images of buried objects [26]. The simulation scenario encompassed a metal cylinder, metal tiffin box, and plastic tiffin box at varying depths, a domain measuring 0.39 meters, 0.10 meters, and 0.20 meters in the x, y, and z-

directions, respectively, and to minimize side wall reflections, an absorbing boundary condition is implemented. The spatial discretization of each cell uses a spacing of 0.002 meters in all three directions (x, y, and z). The source (magnetic dipole) and receiver are at (0.02, 0.05, 0.15) and (0.07, 0.05, 0.15) meters. The source and receiver antennas move together with steps of 0.01 meters in the x-direction. The domain box under the subsurface is defined from (0, 0, 0) to (0.39, 0.1, 0.15) meters as halfspace and airgap region above the ground from (0, 0, 0.15) to (0.39, 0.10, 0.20) meters as free space.

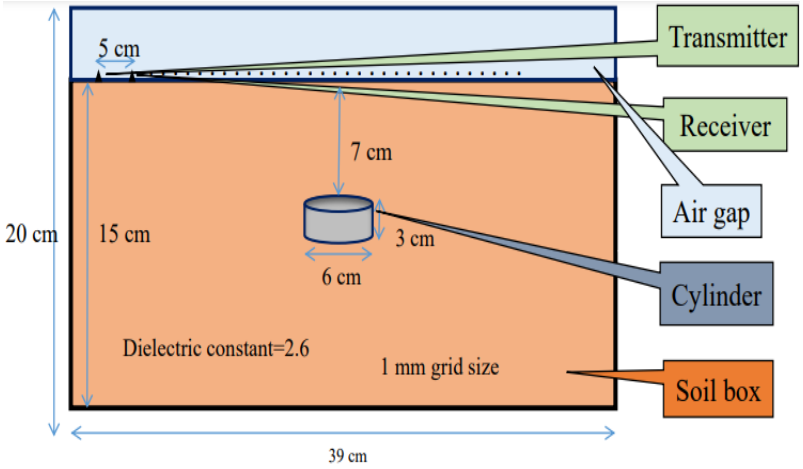


**Figure 2. Simulation Model for Buried Metal Cylinder**

One of the simulation scenarios with a metal cylinder as an object, depicted in Figure 2 with a radius of 0.019 meters, is buried from (0.21, 0.02, 0.05) to (0.21, 0.08, 0.05) meters and modeled as a perfect electric conductor (PEC). We varied the diameter (1 cm to 4 cm) and horizontal placement of cylindrical objects, along with their depth (1 cm to 7 cm) and material properties (relative permittivity: 1 to 20).

The simulation involves gathering 30 A-scans along the scan traces to form a B-scan while also considering three buried objects of different types. A separate B-scan image with no buried objects (background scan) was acquired to account for natural background noise. Figure 3 shows the raw B-Scan images of the buried metal pipe and tiffin box and the plastic tiffin box simulated through the gprMax simulation software [27]. Table 2 summarizes the simulation scenarios, including the types of buried objects, their material properties, diameter range, depth range, relative permittivity, and the corresponding number of B-scans generated for each object type. The process generated 1157 raw B-scan datasets, categorized into three distinct object types.

**Table 2**

**Buried Object Parameter for Simulated Dataset**

| Object Type | Material | Number of B-Scans |
|---|---|---|
| Metal Pipes | PEC | 532 |
| Metal Tiffin Boxes | PEC | 536 |
| Plastic Tiffin Boxes | PVC | 449 |

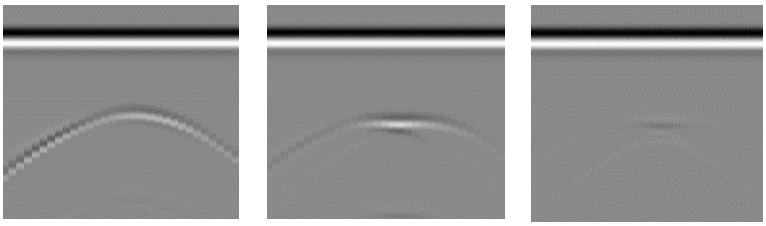

Metal Pipe  Metal Tiffin Box  Plastic Tiffin Box

**Figure 3. Raw B-Scan Images**

### 3.2 Background B-Scan Acquisition

Acquire a separate B-Scan image (background scan) with no buried objects. A background B-Scan image can be acquired in a controlled environment or by identifying an area in the field data free from landmines. Figure 4 represents the B-scan image of background clutter acquired under identical soil conditions without buried objects.

They depict the natural background noise from the ground, transmitter, and receiver antennas without including simulated landmines or other underground objects.

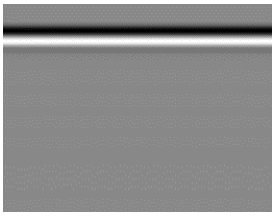

**Figure 4. Background B-Scan Images without buried object**

### 3.3 Clutter-free B-Scan

Background subtraction is a common technique in various imaging applications, including GPR. In the context of landmine detection, background subtraction aims to remove unwanted background noise and reflections from the raw B-Scan image, leaving a clearer picture of potential buried objects. The technique assumes that the background clutter remains relatively constant across different B-Scans collected under similar conditions (same soil properties, antenna configuration, etc.). Performing pixel-wise subtraction entails subtracting the pixel value of each location in the raw B-Scan image (R (x, y)) from its corresponding pixel value in the background B-Scan (B (x, y)). The process yields the clutter-free B-Scan (CF (x, y)) as calculated by Equation 1. The subtraction eliminates standard background noise in both scans, enhancing the clarity of features potentially connected with buried objects in the resulting B-Scan image. Figure 5 illustrates clutter-free B-Scan Images.

$$\mathrm{CF}(x,y) = \mathrm{R}(x,y) - \mathrm{B}(x,y) \quad (1)$$

Metal Pipe Metal Tiffin Box Plastic Tiffin Box

**Figure 5. Clutter-free B-Scan Images**

### 3.4 Pseudocode for CNN and AlexNet-based Image Classification

The system utilizes a CNN architecture, specifically AlexNet, for landmine classification. The pseudocode outlines the general steps for training a CNN/AlexNet on GPR image data, including data loading, network definition, analysis of the network, training options, testing, performance evaluation, and visualization.

| **Pseudocode for Image Classification using CNN and AlexNet** |
|---|
| **1. Load Data** |
| - Load image datastore from data_directory & Split data into training and validation sets |
| **2. Load CNN / Pre-trained Network** |
| - Define CNN / AlexNet architecture |
| **3. Analyze Network Architecture** |
| **4. Define Training Options and Train the Network** |
| - Train CNN/AlexNet on training data with defined options |
| **5. Test the Network** |
| - Make predictions & Calculate accuracy |
| **6. Visualize performance** |
| - Confusion matrix |

MATLAB [28] facilitates deep learning analysis of B-Scan GPR data. This powerful platform offers a comprehensive environment for data manipulation, feature extraction, model development, training, evaluation, and visualization, making it ideal for interpreting GPR data for landmine detection.

### 3.5 CNN Architecture

Figure 6 illustrates the architecture of the simple CNN architecture that takes a grayscale image as input, sized at 521 x 664 x 1 pixels, and processes it through several stages to classify it into different categories. The first three

convolutional layers, each with increasing numbers of filters like 8, 16, and 32, extract progressively more complex features from the image. There can be additional layers, such as batch normalization and Rectified Linear Unit (ReLU) activation, between the convolutional and pooling layers to improve the training speed, introduce non-linearity, and promote sparsity to enhance the overall performance of the CNN. The network utilizes two max-pooling layers to downsample the image size while retaining key features. Finally, a fully connected layer transforms the remaining features into a vector, and a Softmax layer outputs probabilities for each class. Table 3 demonstrates the CNN architecture analysis and its configuration parameters. The confusion matrix is like a scorecard for the image classification model. Each row shows the actual object type buried underground (metal pipe, metal tiffin box, or plastic tiffin box). The columns show what the model predicted each image to be. Ideally, the numbers along the True Positives (TP) diagonal would be high, indicating the model correctly classified many images. False positives (FP) occur when the model makes a confident mistake, such as calling a metal tiffin box a metal pipe. False negatives (FN) are like missed detections, where the model misses the object entirely or assigns it to the wrong class altogether. Figure 7 displays CNN's training progress.

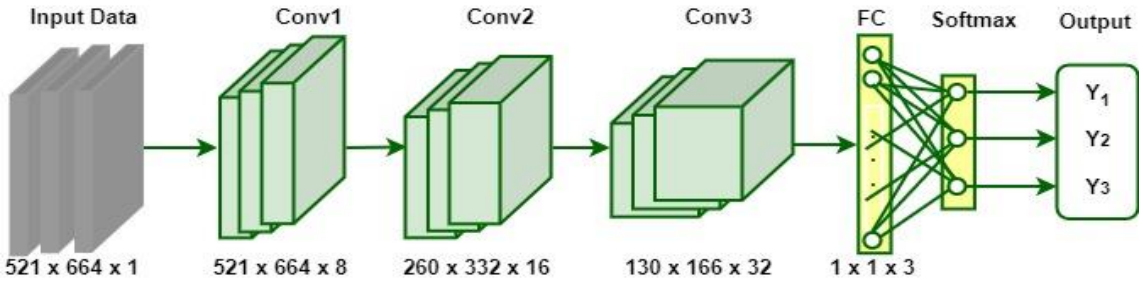


**Figure 6. CNN Architecture**

The loss and accuracy curve visually represents CNN's and AlexNet's progress. Loss curves display the training and validation loss across 10 epochs, indicating the model's learning and generalization performance. Similarly, accuracy curves illustrate the training and validation accuracy over ten epochs (113 iterations per epoch), reflecting the model's classification accuracy. Figure 8 demonstrates the confusion matrix of CNN.

**Table 3**
**CNN architecture analysis and configuration parameters**

| Name | Type | Activations | Learnable Properties |
|---|---|---|---|
| imageinput | Image Input | 521 (S) × 664 (S) × 1 (C) × 1 (B) | - |
| conv_1 | 2-D Convolution | 521 (S) × 664 (S) × 8 (C) × 1 (B) | Weights 3 × 3 × 1 , Bias 1 × 1 × 8 |
| batchnorm_1 | Batch Normalization | 521 (S) × 664 (S) × 8 (C) × 1 (B) | Offset 1 × 1 × 8 , Scale 1 × 1 × 8 |
| relu_1 | ReLU | 521 (S) × 664 (S) × 8 (C) × 1 (B) | - |
| maxpool_1 | 2-D Max Pooling | 260 (S) × 332 (S) × 8 (C) × 1 (B) | - |
| conv_2 | 2-D Convolution | 260 (S) × 332 (S) × 16 (C) × 1 (B) | Weights 3 × 3 × 8 , Bias 1 × 1 × 16 |
| batchnorm_2 | Batch Normalization | 260 (S) × 332 (S) × 16 (C) × 1 (B) | Offset 1 × 1 × 16 , Scale 1 × 1 × 16 |
| relu_2 | ReLU | 260 (S) × 332 (S) × 16 (C) × 1 (B) | - |
| maxpool_2 | 2-D Max Pooling | 130 (S) × 166 (S) × 16 (C) × 1 (B) | - |
| conv_3 | 2-D Convolution | 130 (S) × 166 (S) × 32 (C) × 1 (B) | Weights 3 × 3 × 16 , Bias 1 × 1 × 32 |
| batchnorm_3 | Batch Normalization | 130 (S) × 166 (S) × 32 (C) × 1 (B) | Offset 1 × 1 × 32 , Scale 1 × 1 × 32 |
| relu_3 | ReLU | 130 (S) × 166 (S) × 32 (C) × 1 | - |

| | | | |
|---|---|---|---|
| | | (B) | |
| fc | Fully Connected | 1 (S) × 1 (S) × 3 (C) × 1 (B) | Weights 3 × 690560 , Bias 3 × 1 |
| softmax | Softmax | 1 (S) × 1 (S) × 3 (C) × 1 (B) | - |
| classoutput | Classification Output | 1 (S) × 1 (S) × 3 (C) × 1 (B) | - |

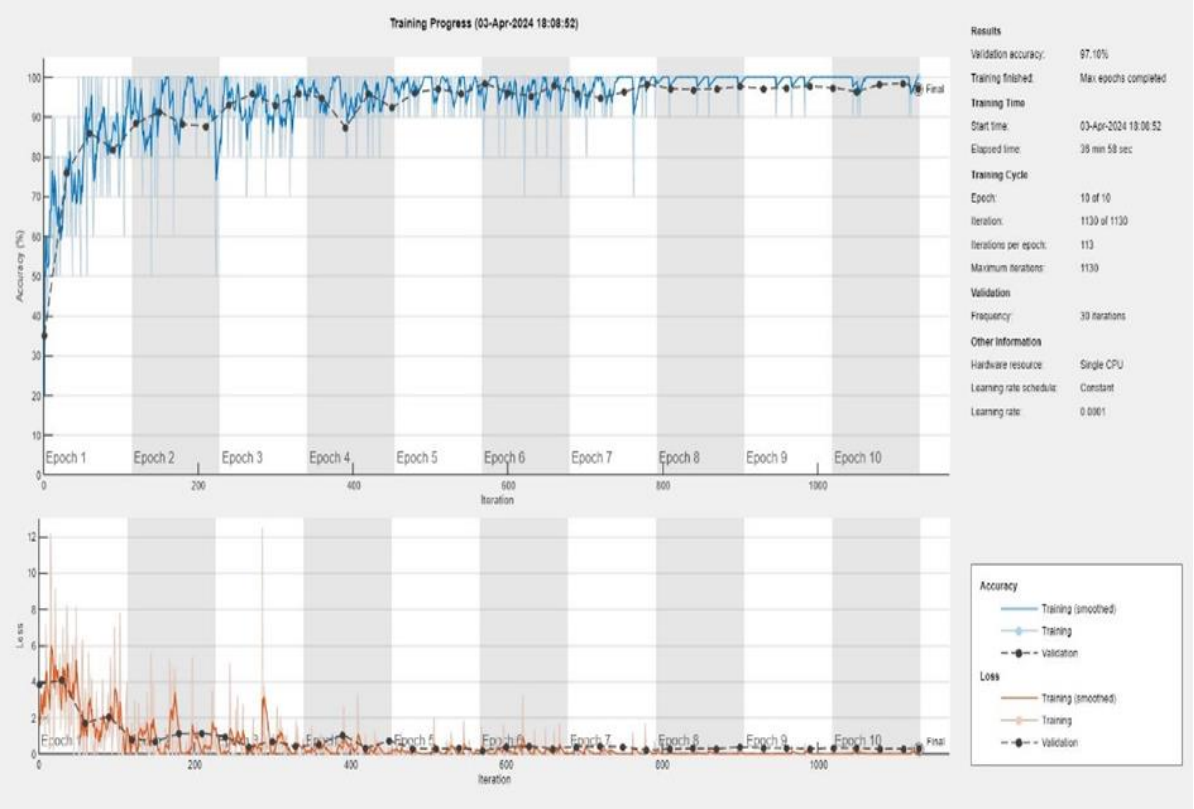


**Figure 7. Training Progress of Convolutional Neural Network**


**Figure 8. Confusion Matrix of Convolutional Neural Network**

### 3.6 Architecture of AlexNet

AlexNet was one of the first CNNs to succeed significantly on a large image classification benchmark dataset

(ImageNet). It paved the way for developing more profound and powerful CNN architectures today in various computer vision tasks. Figure 9 illustrates the architecture of the AlexNet.

The input image of AlexNet architecture, sized at 227 x 227 x 3 pixels, undergoes processing through a network of eight layers, comprising five convolutional layers denoted as Conv1 through Conv5, followed by three fully connected layers labeled FC6 to FC8. In convolutional layers, features are extracted from the image using learnable filters and applied to the previous layer's output to generate feature maps. These filters help detect edges, lines, and other low-level features in the image. ReLU emphasizes them, normalization smooths learning, and pooling shrinks the image while capturing essential details. The fully connected layers take the features from the convolutional layers and convert them into class scores for different categories. The final (FC8) layer outputs the probability distribution for each class, allowing the network to classify the image.

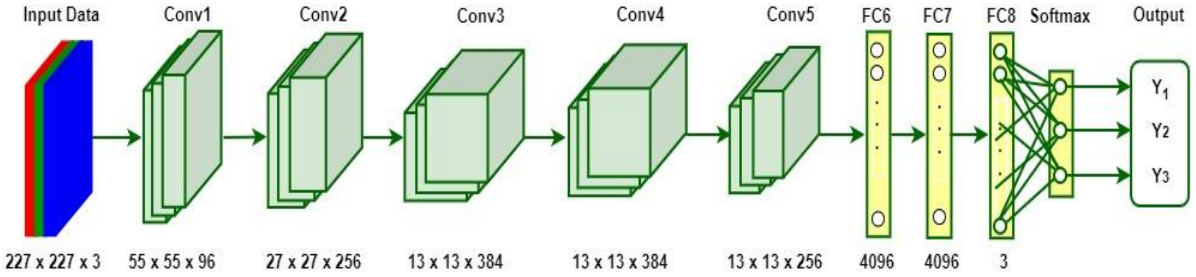


**Figure 9. Architecture of AlexNet**

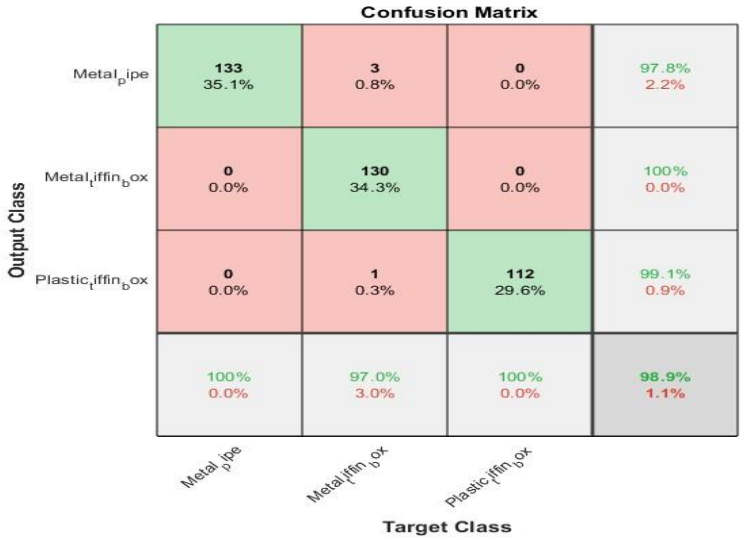


**Figure 11. Confusion Matrix of AlexNet**

Table 4 illustrates the architecture analysis of AlexNet and its configuration parameters. Figure 10 displays AlexNet's training progress. Figure 11 demonstrates the confusion matrix of AlexNet.

**Table 4**

**Architecture analysis of AlexNet and configuration parameters**

| Name | Type | Activations | Learnable Properties |
|---|---|---|---|
| data | Image Input | 227 (S) × 227 (S) × 3 (C) × 1 (B) | - |
| conv1 | 2-D Convolution | 55 (S) × 55 (S) × 96 (C) × 1 (B) | Weights 11 × 11 × 3 , Bias 1 × 1 × 96 |
| relu1 | ReLU | 55 (S) × 55 (S) × 96 (C) × 1 (B) | - |
| norm1 | Cross Channel Normalization | 55 (S) × 55 (S) × 96 (C) × 1 (B) | - |

| | | | |
|---|---|---|---|
| pool1 | 2-D Max Pooling | 27 (S) × 27 (S) × 96 (C) × 1 (B) | - |
| conv2 | 2-D Grouped Convolution | 27 (S) × 27 (S) × 256 (C) × 1 (B) | Weights 5 × 5 × 48 , Bias 1 × 1 × 128 |
| relu2 | ReLU | 27 (S) × 27 (S) × 256 (C) × 1 (B) | - |
| norm2 | Cross Channel Normalization | 27 (S) × 27 (S) × 256 (C) × 1 (B) | - |
| pool2 | 2-D Max Pooling | 13 (S) × 13 (S) × 256 (C) × 1 (B) | - |
| conv3 | 2-D Convolution | 13 (S) × 13 (S) × 384 (C) × 1 (B) | Weights 3 × 3 × 256 , Bias 1 × 1 × 384 |
| relu3 | ReLU | 13 (S) × 13 (S) × 384 (C) × 1 (B) | - |
| conv4 | 2-D Grouped Convolution | 13 (S) × 13 (S) × 384 (C) × 1 (B) | Weights 3 × 3 × 192 , Bias 1 × 1 × 192 |
| relu4 | ReLU | 13 (S) × 13 (S) × 384 (C) × 1 (B) | - |
| conv5 | 2-D Grouped Convolution | 13 (S) × 13 (S) × 256 (C) × 1 (B) | Weights 3 × 3 × 192 , Bias 1 × 1 × 128 |
| relu5 | ReLU | 13 (S) × 13 (S) × 256 (C) × 1 (B) | - |
| pool5 | 2-D Max Pooling | 6 (S) × 6 (S) × 256 (C) × 1 (B) | - |
| fc6 | Fully Connected | 1 (S) × 1 (S) × 4096 (C) × 1 (B) | Weights 4096 × 92 , Bias 4096 × 1 |
| relu6 | ReLU | 1 (S) × 1 (S) × 4096 (C) × 1 (B) | - |
| drop6 | Dropout | 1 (S) × 1 (S) × 4096 (C) × 1 (B) | - |
| fc7 | Fully Connected | 1 (S) × 1 (S) × 4096 (C) × 1 (B) | Weights 4096 × 4096, Bias 4096 × 1 |
| relu7 | ReLU | 1 (S) × 1 (S) × 4096 (C) × 1 (B) | - |
| drop7 | Dropout | 1 (S) × 1 (S) × 4096 (C) × 1 (B) | - |
| fc | Fully Connected | 1 (S) × 1 (S) × 3 (C) × 1 (B) | Weights 3 × 4096 , Bias 3 × 1 |
| softmax | Softmax | 1 (S) × 1 (S) × 3 (C) × 1 (B) | - |
| classoutput | Classification Output | 1 (S) × 1 (S) × 3 (C) × 1 (B) | - |

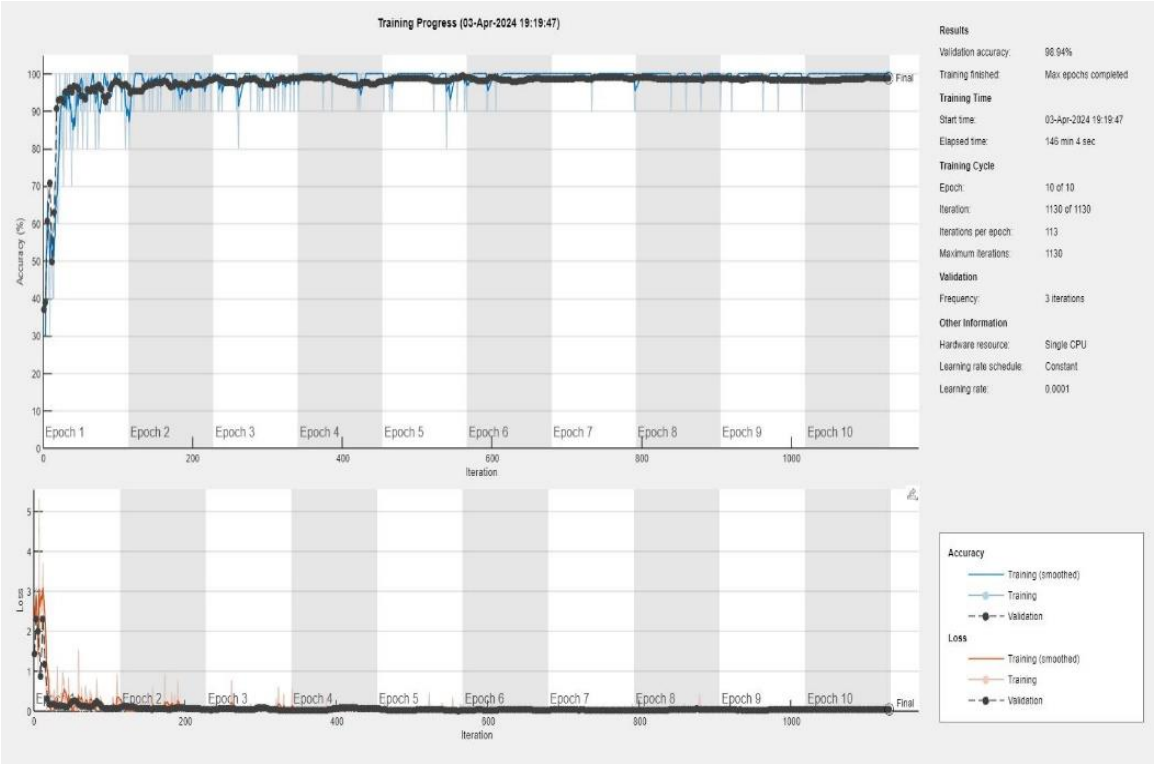


**Figure 10. Training Progress of AlexNet**

## IV. RESULT AND ANALYSIS

We compared the performance of a standard CNN model to AlexNet on a 3-class classification task. The task involved identifying metal pipes and metal and plastic tiffin boxes. We evaluated performance using precision, recall, F1-score, and accuracy metrics.

### 4.1 Precision

Precision measures the exactness of the model's positive predictions for a specific class using Equation 2. A particular class means it tells you what proportion of objects the model identified as a specific class (e.g., metal pipe) was that class. A high precision indicates the model rarely makes mistakes when classifying positive cases.

$$\text{Precision (Metal Pipe)} = \frac{TP_1}{(TP_1 + FP_1)} \quad (2)$$

### 4.2 Recall

Recall is a metric calculated using Equation 3 that is different from precision and reflects the model's ability to catch all relevant instances of a specific class. It emphasizes how well the model identifies all the actual objects belonging to that particular class, highlighting its completeness for a specific category.

$$\text{Recall (Metal Pipe)} = \frac{TP_1}{(TP_1 + FN_1)} \quad (3)$$

### 4.3 F1-Score

We compute the F1-score using Equation 4. These metrics balance precision and recall by taking their harmonic means.

$$F1 - Score\ (Metal\ Pipe) = \frac{(2 \times Precision_1 \times Recall_1)}{(Precision_1 + Recall_1)} \quad (4)$$

### 4.4 Accuracy

Equation 5 defines accuracy as a metric gauging a model's overall performance in correct predictions.

$$\text{Accuracy (Metal Pipe)} = \frac{(TP_1 + TP_2 + TP_3)}{(\text{Total Number of Predictions})} \quad (5)$$

Where $TP_1$ refers to True Positives for metal pipe class, $TP_2$ for metal tiffin box, and $TP_3$ for plastic tiffin box. The performance evaluation of Table 5 compares a CNN and AlexNet for a 3-class image classification task involving metal pipes, metal tiffin boxes, and plastic tiffin boxes. The table shows that AlexNet achieved superior performance across all metrics for metal and plastic tiffin boxes, demonstrating its effectiveness in GPR image classification. The overall accuracy (97.10% for CNN, 98.90% for AlexNet) represents the proportion of images

correctly classified across all three classes. AlexNet outperforms CNN, indicating that it accurately classified a higher percentage of images.

**Table 5**
**Comparison of Classification Performance of CNN and AlexNet**

| 3-Class Classification | Methodology | Precision | Recall | F1-Score | Accuracy |
|---|---|---|---|---|---|
| Existing | Shot Multi-Box Detector (SSD) [29] | 92.77% | 76.61% | 83.92% | - |
| | YOLO v3 [29] | 94.62% | 95.28% | 94.45% | |
| | Grid Images (Cavity) [25] | - | - | - | 92.00% |
| | Grid Images (Pipe) [25] | - | - | - | 98.00% |
| Proposed (CNN) | Metal Pipe | 99.2% | 100% | 99.6% | 97.10% |
| | Metal Tiffin Box | 98.5% | 95.6% | 97.0% | |
| | Plastic Tiffin Box | 98.2% | 100% | **99.1%** | |
| Proposed (AlexNet) | Metal Pipe | 97.8% | 100% | 98.9% | **98.90%** |
| | Metal Tiffin Box | **100%** | **100%** | **100%** | |
| | Plastic Tiffin Box | **99.1%** | **100%** | **99.5%** | |

### 4.5 Findings and Future Enhancements

The limited availability of real GPR data on landmines necessitates exploring methods for incorporating real-world data into the training process. Deep learning approaches using CNNs have shown promise in extracting features and potentially determining the size and shape of buried objects from GPR data. Future research directions include:

- Utilizing pre-trained CNN models like AlexNet for transfer learning to improve target detection accuracy potentially.
- Integrating multiple detection technologies for even more robust and reliable landmine classification.
- Exploring different CNN architectures to identify the most suitable model for landmine classification.

## V. CONCLUSION

This paper investigated the application of deep learning, specifically the AlexNet architecture, for improved landmine classification using GPR images. Our findings demonstrate that AlexNet outperforms a standard CNN model in a 3-class classification task involving metal pipes, metal tiffin boxes, and plastic tiffin boxes.

AlexNet achieved higher overall accuracy and superior precision, recall, and F1-score performance of all three classes compared to CNN. These results highlight the potential of deep learning, particularly CNNs like AlexNet, to revolutionize anti-personnel landmine detection using GPR data. Deep learning offers significant advantages for landmine detection, including increased detection probability, reduced false alarms, and enhanced precision in target positioning.

The success of deep learning in GPR image classification paves the way for developing a fully automated landmine detection system. This research contributes to the ongoing effort to create safer environments for people worldwide. Future research explores different CNN architectures and potentially integrates multiple detection technologies to achieve even more robust and reliable landmine classification.

REFERENCES

[1] United Nations Mine Action Service, *Landmines, Explosive Remnants of War and IED*, 3rd ed. United Nations, 2015.

[2] “Landmine Monitor 2022 - World | ReliefWeb.” https://reliefweb.int/report/world/landmine-monitor-2022

[3] “Landmines: Boost Support for Global Ban Treaty | Human Rights Watch.” https://www.hrw.org/news/2022/11/17/landmines-boost-support-global-ban-treaty

[4] L. Safatly *et al.*, “Detection and classification of landmines using machine learning applied to metal detector data,” *J. Exp. Theor. Artif. Intell.*, vol. 33, no. 2, pp. 203–226, 2021, doi: 10.1080/0952813X.2020.1735529.

[5] "What is Ground Penetrating Radar? (A Complete Guide) - TWI." https://www.twi-global.com/technical-knowledge/faqs/ground-penetrating-radar

[6] Harry M. Jol, *Ground Penetrating Radar Theory and Applications*. Elsevier, 2009.

[7] A. Benedetto, F. Tosti, L. Bianchini Ciampoli, and F. D'Amico, "An overview of ground-penetrating radar signal processing techniques for road inspections," *Signal Processing*, vol. 132, pp. 201–209, 2017, doi: 10.1016/j.sigpro.2016.05.016.

[8] C. Maas and J. Schmalzl, "Using pattern recognition to automatically localize reflection hyperbolas in data from ground penetrating radar," *Comput. Geosci.*, vol. 58, pp. 116–125, 2013, doi: 10.1016/j.cageo.2013.04.012.

[9] Y. Dong and F. Ansari, "Non-destructive testing and evaluation (NDT/NDE) of civil structures rehabilitated using fiber reinforced polymer (FRP) composites," *Serv. Life Estim. Ext. Civ. Eng. Struct.*, pp. 193–222, Jan. 2011, doi: 10.1533/9780857090928.2.193.

[10] L. E. Besaw and P. J. Stimac, "Deep convolutional neural networks for classifying GPR B-scans," *Detect. Sens. Mines, Explos. Objects, Obs. Targets XX*, vol. 9454, p. 945413, 2015, doi: 10.1117/12.2176250.

[11] S. Lameri, F. Lombardi, P. Bestagini, M. Lualdi, and S. Tubaro, "Landmine detection from GPR data using convolutional neural networks," *25th Eur. Signal Process. Conf. EUSIPCO 2017*, vol. 2017-Janua, pp. 508–512, 2017, doi: 10.23919/EUSIPCO.2017.8081259.

[12] M. T. Pham and S. Lefèvre, "Buried object detection from B-scan ground penetrating radar data using Faster-RCNN," *Int. Geosci. Remote Sens. Symp.*, vol. 2018-July, pp. 6804–6807, 2018, doi: 10.1109/IGARSS.2018.8517683.

[13] N. Kim, S. Kim, Y. K. An, and J. J. Lee, "A novel 3D GPR image arrangement for deep learning-based underground object classification," *Int. J. Pavement Eng.*, vol. 22, no. 6, pp. 740–751, 2019, doi: 10.1080/10298436.2019.1645846.

[14] H. Harkat, A. E. Ruano, M. G. Ruano, and S. D. Bennani, "GPR target detection using a neural network classifier designed by a multi-objective genetic algorithm," *Appl. Soft Comput. J.*, vol. 79, pp. 310–325, 2019, doi: 10.1016/j.asoc.2019.03.030.

[15] M. Elsaadouny, J. Barowski, and I. Rolfes, "Extracting the Features of the Shallowly Buried Objects using LeNet Convolutional Network," *14th Eur. Conf. Antennas Propagation, EuCAP 2020*, pp. 7–10, 2020, doi: 10.23919/EuCAP48036.2020.9135701.

[16] U. Ozkaya, F. Melgani, M. Belete Bejiga, L. Seyfi, and M. Donelli, "GPR B scan image analysis with deep learning methods," *Meas. J. Int. Meas. Confed.*, vol. 165, 2020, doi: 10.1016/j.measurement.2020.107770.

[17] F. Hou, W. Lei, S. Li, J. Xi, M. Xu, and J. Luo, "Improved Mask R-CNN with distance guided intersection over union for GPR signature detection and segmentation," *Autom. Constr.*, vol. 121, p. 103414, Jan. 2021, doi: 10.1016/j.autcon.2020.103414.

[18] P. Srimuk, A. Boonpoonga, K. Kaemarungsi, K. Athikulwongse, and S. Dentri, "Implementation of and Experimentation with Ground-Penetrating Radar for Real-Time Automatic Detection of Buried Improvised Explosive Devices," *Sensors*, vol. 22, no. 22, Nov. 2022, doi: 10.3390/S22228710.

[19] H. Wang, S. Ouyang, Q. Liu, K. Liao, and L. Zhou, "Buried target detection method for ground penetrating radar based on deep learning," *J. Appl. Remote Sens.*, vol. 16, no. 01, 2022, doi: 10.1117/1.jrs.16.018503.

[20] N. Barkataki, B. Tiru, and U. Sarma, "A CNN model for predicting size of buried objects from GPR B-Scans," *J. Appl. Geophys.*, vol. 200, no. 2000, pp. 0–2, 2022, doi: 10.1016/j.jappgeo.2022.104620.

[21] M. Wang, D. Hu, J. Chen, and S. Li, "Underground infrastructure detection and localization using deep learning enabled radargram inversion and vision based mapping," *Autom. Constr.*, vol. 154, p. 105004, Oct. 2023, doi: 10.1016/J.AUTCON.2023.105004.

[22] H. Liu, Y. Yue, C. Liu, B. F. Spencer, and J. Cui, "Automatic recognition and localization of underground pipelines in GPR B-scans using a deep learning model," *Tunn. Undergr. Sp. Technol.*, vol. 134, p. 104861, Apr. 2023, doi: 10.1016/J.TUST.2022.104861.

[23] Z. Wang *et al.*, "Unsupervised learning method for rebar signal suppression and defect signal reconstruction and detection in ground penetrating radar images," *Meas. J. Int. Meas. Confed.*, vol. 211, no. July 2022, p. 112652, 2023, doi: 10.1016/j.measurement.2023.112652.

[24] H. Fang, Z. Ma, N. Wang, J. Lei, D. Di, and K. Zhai, "A novel classification method for GPR B-scan images based on weak-shot learning," *J. Appl. Geophys.*, vol. 221, p. 105287, Feb. 2024, doi: 10.1016/J.JAPPGEO.2024.105287.

[25] N. Kim, S. Kim, Y. K. An, and J. J. Lee, "A novel 3D GPR image arrangement for deep learning-based

underground object classification," *Int. J. Pavement Eng.*, vol. 22, no. 6, pp. 740–751, 2021, doi: 10.1080/10298436.2019.1645846.

[26] C. Warren, A. Giannopoulos, and I. Giannakis, "gprMax: Open source software to simulate electromagnetic wave propagation for Ground Penetrating Radar," *Comput. Phys. Commun.*, vol. 209, pp. 163–170, 2016, doi: 10.1016/j.cpc.2016.08.020.

[27] "GitHub - gprMax/gprMax: gprMax is open source software that simulates electromagnetic wave propagation using the Finite-Difference Time-Domain (FDTD) method for numerical modelling of Ground Penetrating Radar (GPR)." https://github.com/gprmax/gprMax

[28] "MATLAB." Accessed: Apr. 07, 2024. https://www.mathworks.com/products/matlab.html

[29] X. Li, H. Liu, F. Zhou, Z. Chen, I. Giannakis, and E. Slob, "Deep learning–based nondestructive evaluation of reinforcement bars using ground-penetrating radar and electromagnetic induction data," *Comput. Civ. Infrastruct. Eng.*, vol. 37, no. 14, pp. 1834–1853, 2022, doi: 10.1111/mice.12798.